

Submitted to AJ

Spectroscopic confirmation of the planetary nebula nature of PM 1-242, PM 1-318 and PM 1-333 and morphological analysis of the nebulae

L. F. Miranda¹*Instituto de Astrofísica de Andalucía, CSIC, Ap. Correos 3004, 18080 Granada, Spain*

lfm@iaa.es

C. B. Pereira²*Observatório Nacional-MCT, Rua José Cristino, 77. CEP 20921-400, São Cristóvão, Rio de Janeiro-RJ, Brasil*

claudio@on.br

M. A. Guerrero¹*Instituto de Astrofísica de Andalucía, CSIC, Ap. Correos 3004, 18080 Granada, Spain*

mar@iaa.es

ABSTRACT

We present intermediate resolution long-slit spectra and narrow-band $H\alpha$, $[N\ II]$ and $[O\ III]$ images of PM 1-242, PM 318 and PM 1-333, three IRAS sources classified as possible planetary nebulae. The spectra show that the three objects are true planetary nebulae and allow us to study their physical properties; the images provide a detailed view of their morphology. PM 1-242 is a medium-to-high-excitation (e.g., $He\ II\lambda 4686/H\beta \sim 0.4$; $[N\ II]\lambda 6584/H\alpha \sim 0.3$) planetary nebula with an elliptical shape containing $[N\ II]$ enhanced point-symmetric arcs. An electron temperature $[T_e([S\ III])]$ of $\sim 10250\ K$ and an electron density $[N_e([S\ II])]$ of $\sim 2300\ cm^{-3}$ are derived for PM 1-242. Abundance calculations suggest a large helium abundance ($He/H \sim 0.29$) in PM 1-242. PM 1-318 is a high-excitation ($He\ II\lambda 4686/H\beta \sim 1$) planetary nebula with a ring-like inner shell containing two enhanced opposite regions, surrounded by a fainter round attached shell brighter in the light of $[O\ III]$. PM 1-333 is an extended planetary nebula with a high-excitation ($He\ II\lambda 4686/H\beta$ up to ~ 0.9) patchy circular main body containing two low-excitation knotty arcs. A low $N_e([S\ II])$ of $\sim 450\ cm^{-3}$ and $T_e([O\ III])$ of $\sim 15000\ K$ are derived for this nebula. Abundance calculations suggest that PM 1-333 is a type I planetary nebula. The lack of a sharp shell morphology, low electron density, and high-excitation strongly suggest that PM 1-333 is an evolved planetary nebula. PM 1-333

also shows two low-ionization polar structures whose morphology and emission properties are reminiscent of collimated outflows. We compare PM 1-333 with other evolved planetary nebulae with collimated outflows and find that outflows among evolved planetary nebulae exhibit a large variety of properties, in accordance with these observed in younger planetary nebula.

Subject headings: planetary nebula: individual (PM 1-242, PM 1-318, PM 1-333) – ISM: jets and outflows – circumstellar matter

1. Introduction

Planetary nebulae (PNe) represent the last evolutionary stage of low- and intermediate-mass ($M \leq 8 M_{\odot}$) stars before they enter the white dwarf phase, forming from Asymptotic Giant Branch (AGB) stars after a short post-AGB phase (Bloeker 1995). Both the stellar and circumstellar properties dramatically change during the AGB to PN transition (e.g., Balick & Frank 2002). A precise knowledge of the processes involved in this transition relies in the identification of a large number of these objects in order to establish possible connections and evolutionary paths from the AGB to the PN phase. Identification of candidate post-AGB stars and PNe has been successful using the IRAS [12]–[25] vs. [25]–[60] two colour diagram (Preite-Martínez 1988; García-Lario et al. 1997). In this diagram, these objects are located in a well defined region marked by two lines delimited by $[12] - [25] \geq 0.75$ and $[25] - [60] \leq 1.13$ (see García-Lario et al. 1997; Pereira & Miranda 2007). However, this region overlaps with those of OH/IR stars, young stellar objects and H II regions. Therefore, the IRAS two colour diagram does not provide an unambiguous identification of post-AGB stars and PNe.

Recently, we have started a spectroscopic program to establish the true nature of sources classified as possible post-AGB stars and PNe on the basis of their IRAS colours. We have already identified six new post-AGB stars, two H II regions, several objects of other different nature (Pereira & Miranda 2007), and a new high density young PN, PM 1-322, that could host a symbiotic star (Pereira & Miranda 2005). As PM 1-322 is located in a region of the IRAS two colour diagram that is common to post-AGB stars, PNe, OH/IR stars and young stellar objects, spectroscopy has been decisive to achieve an unambiguous classification.

In the framework of this spectroscopic program, we have also investigated the true nature of PM 1-242, PM 1-318 and PM 1-333, three objects classified in SIMBAD as *possible planetary nebulae* mainly based in their IRAS colours. Table 1 provides the names, coordinates and IRAS colours for these three objects. The three are located in a region of the IRAS two colour diagram in which PNe overlap with objects of different nature. In particular, it cannot be ruled out the possibility of PM 1-242 and PM 1-318 being compact H II regions (see Fig. 1 in Pereira & Miranda 2007). PM 1-242 has been detected in the objective-prism survey of H α emission objects by Robertson & Jordan (1989, their object 104). However, its detection in H α does not guarantee a PN nature.

For PM 1-318 there is no additional information available to investigate its true nature. Finally, in the case of PM 1-333, radio continuum emission at 1.4 GHz and He II $\lambda 4686$ line emission have been detected from the nebula (Condon et al. 1999), which does favor a PN classification. Nevertheless, a detailed analysis of the spectrum of PM 1-333 has not been carried out as it is the case of PM 1-242 and PM 1-318 for which no spectra are available. In order to establish the nature of these objects, spectroscopic observations are a first crucial step.

The morphology of these three objects has neither been analyzed. In the POSS, PM 1-242 appears stellar, PM 1-318 appears as a very small and tenuous nebulosity, and PM 1-333 appears as a faint extended nebula. In none of the cases, details about the internal structure can be recognized in the POSS. Although morphology cannot be used as an indicator of the nature of a nebula, it is true that PNe and nebulae around post-AGB stars exhibit much more symmetric (or axisymmetric) shapes than H II regions (Manchado et al. 1996; Sahai & Trauger 1998; Sahai et al. 2007). Furthermore, many PNe present small scale regions of high $[\text{N II}]/\text{H}\alpha$ ratios (≥ 1) (e.g., Balick et al. 1994) that cannot be attained in young stellar objects and H II regions. Therefore, the presence of bright $[\text{N II}]$ regions in a nebula can be indicative of a PN nature (e.g., Miranda et al. 1998). Thus images obtained in $[\text{N II}]$ and $\text{H}\alpha$ filters may be useful to assess the nature of a nebula.

In this paper, we present intermediate-resolution spectra and narrow-band optical images of PM 1-242, PM 1-318 and PM 1-333. These observations have allowed us to confirm that they are true PNe, and to investigate their physical conditions and morphology.

2. Observations

2.1. Spectroscopy

Long-slit spectroscopic observations were obtained in 2005 August 3 and 5 using the Calar Alto Faint Object Spectrograph (CAFOS) at the 2.2 m telescope on Calar Alto Observatory¹ (Almería, Spain). The detector was a SiTe CCD with 2048×2048 pixels. The gratings B-100 and R-100 were used to cover the spectral ranges 3200–6200 Å and 5800–9600 Å, respectively. In both spectral ranges, the dispersion was $\simeq 2 \text{ Å pixel}^{-1}$. The spatial scale on the detector is $0.53 \text{ arcsec pixel}^{-1}$. The slit width was $4''$ and it was oriented North-South and centered in the objects; in the case of PM 1-333, an additional red spectrum was obtained with the slit offset $27''$ toward the West from the nebular center. The exposure time for both spectral ranges was 1800 s in the cases of PM 1-242 and PM 1-318, 2700 s for the spectra of the central region of PM 1-333, and 3600 s for the off-center spectrum of PM 1-333. Spectrophotometric standards from Oke (1974) and Massey et al. (1988) were observed for flux calibration. As the sky was clear but no photometric during the observations, the absolute fluxes must be used with caution. The data were reduced using standard procedures

¹The Centro Astronómico Hispano-Alemán at Calar Alto is operated jointly by the Max-Planck-Institut für Astronomie and the Instituto de Astrofísica de Andalucía (CSIC).

within the IRAF² package.

2.2. Imaging

Narrow-band direct images of PM 1-242, PM 1-318 and PM 1-333 were obtained in 2005 August 3 and 2006 June 29 using ALFOSC at the Nordic Optical Telescope³ on Roque de los Muchachos Observatory (La Palma, Spain). The detector was an E2V CCD with 2048×2048 pixels and a plate scale of 0.19'' pixel⁻¹. Images were obtained through three narrow-band filters: H α ($\lambda_c = 6563$ Å, FWHM = 9 Å), [N II] ($\lambda_c = 6584$ Å, FWHM = 9 Å) and [O III] ($\lambda_c = 5007$ Å, FWHM = 30 Å). Exposure time was 1800 s for each filter. Seeing was $\simeq 1''$ during the observations. In the case of PM 1-333, an additional image in the Johnson R filter was obtained during the acquisition of the spectra on 2005 August 3, with an exposure time of 300 s and a seeing of $\simeq 1.2''$. The images were reduced following standard procedures within the MIDAS package.

3. Results

Figure 1 shows the blue and red spectra of PM 1-242, PM 1-318 and PM 1-333. The spectra of PM 1-242 and PM 1-318 in Fig. 1 have been obtained from the respective long-slit spectra by integrating over the total spatial extent of these two (relatively small) objects (see §3.1 and §3.2). In PM 1-333, the spectra in Fig. 1 correspond to two nebular regions of different emission properties extracted from the long-slit spectrum acquired with the slit going through the nebular center (see §3.3). All the spectra in Fig. 1 are typical of ionized nebulae, showing emission lines of recombination H and He transitions, forbidden lines of various ionization states and weak continuum emission. Table 2 presents the underreddened line intensities together with their Poissonian errors. The line intensities have been underreddened using the extinction law of Seaton (1979) and the logarithmic extinction coefficient $c_{H\beta}$ (see Table 2) derived from the observed H α /H β ratio assuming Case B recombination ($T_e = 10^4$ K, $N_e = 10^4$ cm⁻³) for the theoretical Balmer line ratio of 2.85 (Brocklehurst 1971).

The line intensities listed in Table 2 show high He II $\lambda 4686$ /H β and [O III] 5007/H β line ratios between 0.4 – 1.1 and 5 – 15, respectively. These high line ratios are not seen in H II regions and young stellar objects. On the contrary, they are typical of PNe. Therefore, the spectra of these three objects strongly point to a PN nature. Accordingly, we apply to these objects the PNG

²IRAF is distributed by the National Optical Astronomy Observatory, which is operated by the Association of Universities for Research in Astronomy (AURA) under cooperative agreement with the National Science Foundation.

³Based on observations made with the Nordic Optical Telescope, operated on the island of La Palma jointly by Denmark, Finland, Iceland, Norway, and Sweden, in the Spanish Observatorio del Roque de los Muchachos of the Instituto de Astrofísica de Canarias.

designation of PNe (Acker et al. 1992): PN G031.1+03.7, PN G074.5+02.3 and PN G100.4+04.6 for PM 1-242, PM 1-318 and PM 1-333, respectively (see Table 1). In the following, we will describe the spectra and images of each object in more detail.

3.1. PM 1-242

Figure 2 shows the $H\alpha$, $[N\ II]$ and $[O\ III]$ images of PM 1-242. The object presents an elliptical morphology with the major axis oriented almost along the North-South direction, and a size of $\simeq 8'' \times 5''$ in $[N\ II]$ and somewhat smaller in $H\alpha$ and $[O\ III]$. Two bright knots define the minor axis of the ellipse in the $H\alpha$ and $[O\ III]$ images, with point-symmetric arcs emanating from these knots and tracing the ellipse. The point-symmetric intensity distribution is particularly marked in $[N\ II]$. At low intensity levels, the $H\alpha$ and $[O\ III]$ images show protrusions along $PA \simeq 50^\circ$ – 230° and $PA \simeq 150^\circ$ (see inset in the $H\alpha$ image of Fig. 2). In addition, an isolated knot is observed in the three filters at $9.1''$ from the center along $PA \simeq 225^\circ$. Fig. 2 also shows the $[N\ II]/[O\ III]$ ratio map of PM 1-242 constructed in order to analyze the excitation within the object. The lowest excitation is observed around the polar regions of the ellipse, in particular, in two point-symmetric arcs. The central region and bright knots along the minor axis show the highest excitation, while the isolated knot outside the main body of the nebula presents intermediate excitation.

The spectrum of PM 1-242 (Fig. 1) shows relatively strong $He\ II$ and $[O\ III]$ emissions ($He\ II\lambda 4686/H\beta \simeq 0.43$; $[O\ III]\lambda 5007/H\beta \simeq 15$) and relatively weak $[N\ II]$ and $[S\ II]$ emissions ($[N\ II]\lambda 6584/H\alpha \simeq 0.31$; $[S\ II]\lambda\lambda 6716, 6731/H\alpha \simeq 0.08$). These line intensity ratios indicate a medium-to-high excitation PN. We note that variations of the line intensity ratios within the nebula should exist as indicated by the $[N\ II]/[O\ III]$ ratio map (Fig 2). In particular, the $[N\ II]\lambda 6584/H\alpha$ ratio in the point-symmetric arcs is probably larger than 0.31. From the $[S\ II]\lambda 6731/\lambda 6716$ line intensity ratio, we derive an electron density (N_e) of $2300 \pm 660\ cm^{-3}$. The non detection of the $[O\ III]\lambda 4363$ and $[N\ II]\lambda 5775$ emission lines does not allow us to determine the electron temperature (T_e) for these ions. Using the $[S\ III]$ auroral and nebular lines detected in the spectrum, we obtain $T_e = 10250 \pm 690\ K$.

Chemical abundances in PM 1-242 have been derived assuming the values of T_e and N_e quoted above. Ionic abundances are listed in Table 3 and have been obtained using the task IONIC in the IRAF package. The errors in the ionic abundances account for the uncertainties in the line intensities and in the determination of the physical parameters. These errors are relatively high, particularly in the case of O^+ ($\sim 60\%$). Elemental abundances are listed in Table 4 and have been obtained using the ionization correction factors (icf) of Kingsburgh & Barlow (1994). Table 4 also lists elemental abundances in other objects for comparison purposes. PM 1-242 presents a high helium abundance ($He/H \simeq 0.29$) that is well determined with an error of $\sim 10\%$. This result suggests that PM 1-242 is a type I PN although the N/O ratio of $\simeq 0.22$ is unusually low for a type I PN (Peimbert 1990; see Table 4). Note, however, that the errors in the ionic abundances of O^+ and N^+ (Table 3) are large, and a N/O ratio of up to $\simeq 0.7$ is consistent with the observations, making this value typical of type I PNe. A more accurate determination of the N/O ratio in this

PN is most needed.

3.2. PM 1-318

$H\alpha$ and $[O\text{ III}]$ images of PM 1-318 are shown in Figure 3 together with an $[O\text{ III}]/H\alpha$ image ratio derived to study the excitation within the object. The $[N\text{ II}]$ image is not shown because of the extreme weakness of the $[N\text{ II}]$ emission (see below). PM 1-318 presents the morphology of a circular ring with a diameter of $\simeq 3.5''$ and a thickness of $\simeq 1.5''$, surrounded by an attached round shell with a diameter of $\simeq 10''$ in $[O\text{ III}]$ and slightly smaller ($\simeq 9''$) in $H\alpha$. The ring contains two bright regions separated $\simeq 3.2''$ along $PA \simeq 35^\circ$. The $[O\text{ III}]/H\alpha$ image ratio shows that the attached shell presents higher excitation than the inner nebular regions.

The spectrum of PM 1-318 is characterized by strong high-excitation lines and very faint low-excitation emissions (Fig. 1 and Table 2). In particular, $He\text{ II}$ emissions are strong (e.g., $He\text{ II}\lambda 4686/H\beta \simeq 1.1$). Other high-excitation emissions include $[Ar\text{ V}]$ and $[Cl\text{ IV}]$ lines. However, the $[O\text{ III}]$ emissions are moderate ($[O\text{ III}]\lambda 5007/H\beta \simeq 5.5$) and the $[O\text{ III}]\lambda 4363$ line is not detected, suggesting relatively large amounts of O^{+3} in the nebula. The $[N\text{ II}]$ emissions are very weak ($[N\text{ II}]\lambda 6584/H\alpha \simeq 0.01$) and $[S\text{ II}]$, $[O\text{ I}]$ and $[O\text{ II}]$ emissions are absent. These results allow us to classify PM 1-318 as a double shell high-excitation PN.

3.3. PM 1-333

3.3.1. Morphology

Figure 4 shows the $H\alpha$, $[N\text{ II}]$, $[O\text{ III}]$ and R images of PM 1-333. The images show an extended nebula that is brighter in the light of $[O\text{ III}]$, somewhat fainter in the light of $H\alpha$, and that shows a very different morphology in the light of $[N\text{ II}]$. All the images, in particular the R one, show a faint star located close to the geometrical center of the nebula, which may be considered as candidate to the central star of PM 1-333. In the following, we will adopt this star as the origin for radial distances and PAs measurements. We note that PM 1-333 is projected toward the young open cluster Trumpler 37. This coincidence has allowed us to derive an R magnitude of $\simeq 17.8$ mag for the candidate central star by comparing it to the star Cl Trumpler 37 Kun 99 (Kun 1986) which is registered in our R image.

The $[O\text{ III}]$ image shows a nebula of $\simeq 105'' \times 50''$ in size elongated along $PA \simeq 80^\circ$. The main body of the nebula is almost circular with a size between $46''$ and $50''$. No sharp inner or outer edge indicative of a shell structure is observed. The emission from this region is patchy and particularly bright in two knotty arcuate regions, one extending approximately North-South and one extending almost East-West. The morphology of the main body in $H\alpha$ is similar to that in $[O\text{ III}]$, although its extension is slightly smaller. In $[N\text{ II}]$ only the two arcuate regions can be identified, while the

diffuse emission is not detected.

The [N II] image also reveals the presence of two knotty low-ionization structures (LIS) along $PA \simeq 70^\circ$. The SW LIS is brighter than its NE counterpart and it extends closer (between $24''$ and $37''$) to the center of the nebula than the NE LIS (between $34''$ and $43''$). Moreover, the morphology of both LIS is very different from each other: the SW LIS appears as a knotty filament elongated along $PA \simeq 205^\circ$, while the NE LIS is composed of several individual knots. These LIS are associated to bright $H\alpha$ and [O III] extensions protruding from the central region. It is tempting to state that the [N II] bright knots are located at the tip of these high-excitation extensions, but a close inspection reveals that they are rather embedded within the high-excitation extensions. Furthermore, faint [O III] and $H\alpha$ emissions are detected beyond these LIS, although along $PA \simeq 80^\circ$, slightly different from the $PA \simeq 70^\circ$ orientation of the LIS.

The ionization structure of PM 1-333 is illustrated in Figure 5 where we present a colour composite picture constructed with the images in Fig. 4. This colour picture reveals that [O III] dominates in the outer regions of the main body of the nebula while $H\alpha$ emission fills the central regions. Moreover, the bright [N II] emission of the arcuate structures appears embedded within regions of high excitation. We also note that some of the knots in the arcuate structures present radial tails that are better seen in the [N II] emission (red in Fig. 5). In this figure, the LIS appear embedded within regions of high-excitation.

3.3.2. Spectral analysis

As already mentioned, spectra of PM 1-333 were obtained through two different slit positions. The positions of these slits are overlaid on the R image of the nebula in Fig. 4; a slit goes through the center of the nebula close to, but not including, the candidate central star, and the other slit covers the SW LIS. In the latter position, only a red spectrum was obtained. We will concentrate firstly on the spectrum of the main nebular body.

The slit going through the center covers the low ionization arcuate structure toward the South, as well as the nebular regions toward the North where no [N II] is detected in the images. Consequently, we have extracted from the long-slit spectrum two one-dimensional spectra corresponding to the northern region, called PM 1-333 (N), and to the southern arcuate structure, called PM 1-333 (S). The spatial sizes of these regions are $21''$ and $29''$, respectively. These spectra are shown in Fig. 1 (see also Table 2). In PM 1-333 (N), no low-ionization lines are observed, except for some faint [N II] emissions due to contamination from a low-ionization knot. In contrast, relatively strong [O I], [O II], [S II] and [N II] emissions are observed in PM 1-333 (S). The intensity of the He II lines, relative to $H\beta$, is higher in PM 1-333 (N) than in PM 1-333 (S), as it is the case of the high-excitation [Ar IV] $\lambda 4740$ line. He I emissions are observed in PM 1-333 (S) but not in PM 1-333 (N). Other medium-to-high-excitation lines ([O III], [S III], [Ne III] and [Ar III]) are observed in the two regions but their intensity is relatively higher in PM 1-333 (S) than in PM 1-333 (N). In particular, the

[O III] λ 5007/H β intensity ratio is high, $\simeq 12$, in PM 1-333 (S) but moderate, $\simeq 6$, in PM 1-333 (N). These results point out that the excitation level in PM 1-333 (N) is high enough for O $^{+3}$, Ne $^{+3}$, Ar $^{+3}$ and S $^{+3}$ to be the prevalent ionization states. In PM 1-333 (S), the arcuate filament preserves a lower excitation level and, therefore, larger amounts of O $^{+2}$, Ne $^{+2}$, Ar $^{+2}$ and S $^{+2}$.

The auroral [N II] λ 5755, [O III] λ 4363 and [S III] λ 6312 emission lines detected in PM 1-333 (S) allow us to derive values for the electron temperature: $T_e(\text{[N II]}) = 17600 \pm 620$ K, $T_e(\text{[O III]}) = 15300 \pm 225$ K and $T_e(\text{[S III]}) = 22300 \pm 1900$ K. A rather low N_e of 445 ± 45 cm $^{-3}$ is derived from the [S II] line intensity ratio. This value corresponds to the electron density of the low ionization arcuate structure, not to the surrounding higher excitation material in which the electron density is probably lower.

Chemical abundances for PM 1-333 (S) have been derived using the task IONIC in IRAF and the icf of Kingsburg & Barlow (1994), assuming $N_e = 445 \pm 45$ cm $^{-3}$ and $T_e = 15300 \pm 225$ K. The derived ionic and elemental abundances are listed in Table 3 and Table 4, respectively. Errors in the ionic abundances are $\leq 10\%$. In consequence, errors in elemental abundances are estimated to be 20% – 40%. The relatively high helium abundance (He/H $\simeq 0.13$) and high N/O ratio ($\simeq 0.6$) point out to a type I PN (Peimbert 1990; Stanghellini et al. 2006), although the total abundances of N, O, Ne, Ar and S appear lower than the average in PNe (see Kingsburgh & Barlow 1994).

Finally, the red spectrum obtained through the SW LIS (see Fig. 4) is shown in Figure 6. The underreddened line intensities are listed in Table 2 and have been derived assuming that the logarithmic extinction coefficient in the SW LIS is identical to this in PM 1-333 (S) ($c_{H\beta} = 1.19$, see Table 2). We note that the derived line intensity ratios do not critically depend on the assumed value of $c_{H\beta}$. The spectrum of the SW LIS is characterized by very strong low-excitation emissions. The intensities of the [N II], [O I], [O II], and [S II] emissions relative to H α are higher by a factor $\simeq 3$ in the SW LIS than in the arcuate structure. High-excitation emissions of [Ne III] and [Ar III] are also observed in the SW LIS with a relative intensity comparable to or higher than those observed in the main nebular body. These emissions probably arise in the high-excitation material in which the SW LIS is embedded. The electron density in the SW LIS, derived from the [S II] line intensity ratio, is $\simeq 55$ cm $^{-3}$, at the low density limit of the [S II] intensity ratio and lower than the electron density derived above for the arcuate structure. The electron temperature, derived from the [S III] line intensity ratio, is 13500 ± 1600 K, lower than the $T_e(\text{[S III]})$ derived in the main nebular body.

4. Discussion and conclusions

We have presented intermediate-resolution long-slit spectra and narrow-band direct images of three objects classified in SIMBAD as possible PNe: PM 1-242, PM 1-318 and PM 1-333. For PM 1-242 and PM 1-318, evidence for their real nature was lacking. For PM 1-333, the detection of radio continuum emission and He II line emission suggested a PN nature (Condon et al. 1999) but a detailed study of the object was not available.

The spectral properties of PM 1-242, PM 1-318 and PM 1-333 described in §3 confirm that they are indeed PNe. PM 1-242 presents both high- and low-ionization line emissions typical of a medium-to-high-excitation PN. PM 1-318 exhibits a high-excitation spectrum with strong He II and [Ar V] line emissions and extremely weak or absent low-ionization emissions. Finally, PM 1-333 presents regions with different excitation: high-excitation in the main nebular body and low-excitation in two polar structures and two arcs embedded in the main nebular body.

PM 1-242 exhibits an elliptical morphology with two point-symmetric, low ionization [N II] enhanced arcs tracing the ellipse. The physical structure of PM 1-242 could be an ellipsoid, with the major axis along the North-South direction, containing two bright point-symmetric arcs and a bright, high excitation equatorial region. In this case, the physical structure of PM 1-242 would be similar to this of Cn 3-1 as shown by studies of its internal kinematics (Miranda et al. 1997). Alternatively, the faint protrusions observed in the H α and [O III] images suggest that PM 1-242 could be a bipolar PN with its bipolar axis along the East-West direction. The bright ellipse can then be interpreted as a tilted equatorial ring while the faint protrusions (and the isolated knot) would trace faint bipolar extensions. The ring-like structure of PM 1-242 would be then similar to this of, e.g., He 2-428 (Manchado et al. 1996), IC 2149 (Vázquez et al. 2002) or Me 1-1 (Pereira et al. 2008). These PNe present the same basic structure consisting in a bright equatorial ring accompanied by faint bipolar extensions, the difference among them being the orientation of the ring axis (or bipolar axis) with respect to the observer. A study of the internal kinematics of PM 1-242 would certainly allow us to determine the real structure of PM 1-242.

PM 1-318 consists of a ring-like inner shell containing two enhanced opposite regions, surrounded by a fainter circular attached shell. The attached shell presents higher excitation than the inner one. The morphology of PM 1-318 is similar to this of, e.g., NGC 6826, NGC 3242 (Balick et al. 1998) and M 2-2 (Manchado et al. 1996). The circular morphology of the inner shell suggests that PM 1-318 is a round PN. Nevertheless, it cannot be ruled out that the inner shell is elliptical with the major axis tilted with respect to the line of sight.

PM 1-333 is probably an evolved PN, as strongly pointed out by the data presented in this paper. The absence of a sharp shell morphology suggests that the fast wind from the central star has ceased and that the nebular material is backfilling the central cavity. The evolved nature is further confirmed by the high-excitation of the nebula, suggesting a high temperature for the central star, and by the low nebular electron density. In this context, the bright low ionization arcs may represent relics of presumably dense, low ionization structures that were previously present in the nebula. The arcuate morphology of these low ionization structures suggests that they may have been tracing a ring or filamentary structures as those seen in NGC 6543 (Miranda & Solf 1992; Balick & Hajian 2004). The LIS present the properties observed in FLIERs of PNe (Balick et al. 1998). The morphological differences between the SW LIS and the NE LIS compare to these observed in NGC 7009 in which the FLIERs exhibit different morphologies and contain knots oriented at different directions with respect to the central star (Balick et al. 1998). The LIS strongly suggest that collimated outflows are present in PM 1-333. Moreover, the protrusions connecting the

LIS to the main nebular body point out that the collimated outflows have interacted with nebular material in the main nebular body deforming an original round shell. An analysis of the internal kinematics of PM 1-333 would be very valuable in order to study the formation processes of this interesting PN.

Although collimated outflows are usually observed in PNe, there are only a few cases of evolved PNe in which these structures have been detected. In this respect, PM 1-333 can be compared to NGC 1360 (Goldman et al. 2004), Wray 17-4 and K 1-2 (Corradi et al. 1999). These four PNe present a patchy main body with no sharp shell morphology, indicative of evolved PNe, and collimated structures characterized by enhanced $[\text{N II}]$ emission. However, the four cases exhibit noticeable differences. The main shell is approximately circular in Wray 17-4 and PM 1-333 and elliptical in NGC 1360 and K 1-2. The collimated structures are embedded in the main shell of Wray 17-4 and K 1-2, outside the main shell but connected to it in PM 1-333, whereas in NGC 1360 the collimated structures are outside the main shell but not connected to it. The orientation of the outflows relative to that of the main shell is also different in each object. In NGC 1360, the outflows are oriented along the major axis of the elliptical shell, in K 1-2 they are oriented almost perpendicular the main axis of the shell, while in PM 1-333 and Wray 17-4 no orientation can be established for their circular shells. As for the kinematics, the outflows in Wray 17-4 and K 1-2 seem to share the kinematics of the shell while in NGC 1360 they present radial velocities larger than the shell. These results show that collimated outflows in evolved PNe present the same varied phenomenology as those observed in younger PNe (see, e.g., Sahai & Trauger 1998, Miranda et al. 1999, Guerrero et al. 2008, and references therein). This variety is probably related to the different physical processes involved in the formation of PNe.

We thank an anonymous referee for comments that have improved the presentation and discussion of the data. We are grateful to the staff of the NOT and Calar Alto observatories for their help during the observations. This work has been supported partially by grants AYA2005-01495 of the Spanish MEC and AYA2008-01934 of the Spanish MICINN (co-funded by FEDER funds), and by grant FGM-1747 of the Junta de Andalucía. This research has made use of the SIMBAD database, operated at CDS, Strasbourg, France.

REFERENCES

- Acker, A., Marcout, J., Ochsenbein, F., Stenholm, B., Tylenda, R. 1992, Strasbourg - ESO catalogue of galactic planetary nebulae, Garching: European Southern Observatory
- Balick, B., Alexander, J., Hajian, A. R., Terzian, Y., Perinotto, M., & Patriarchi, P. 1998, *AJ*, 116, 360
- Balick, B., & Frank, A. 2002, *ARA&A*, 40, 439
- Balick, B., & Hajian, A.R. 2004, *AJ*, 127, 2269

- Balick, B., Perinotto, M., Maccioni, A., Terzian, Y., & Hajian, A. 1994, *AJ*, 424, 800
- Bloeker, T. 1995, *A&A*, 299, 755
- Brocklehurst, M. 1971, *MNRAS*, 153, 471
- Condon, J.J., Kaplan, D.L., & Terzian, Y. 1999, *ApJS*, 123, 219
- Corradi, R.L.M., Perinotto, M., Villaver, E., et al. *ApJ*, 523, 721
- García-Lario, P. Manchado, A., Pych, W., & Pottasch, S.R. 1997, *A&AS*, 126, 479
- Goldman, D.B., Guerrero, M.A., Chu, Y.-H., & Gruendl, R.A. 2004, *AJ*, 128, 1711
- Guerrero, M.A., Miranda, L.F., Riera, A., et al. 2008, *ApJ*, 693, 272
- Grevesse, N., Asplund, M., & Sauval, A.J. 2007, *Space Sci. Rev.*, 130, 105
- Henry, R.B.C., Kwitter, K.B., & Balick, B. 2004, *AJ*, 127, 2284
- Kingsburgh, R.L., & Barlow, M.J. 1994, *MNRAS*, 295, 75
- Kun, M. 1986, *Ap&SS*, 125, 13
- Manchado, A., Guerrero, M.A., Stanghellini, L., & Serra-Ricart, M. 1996, *The IAC morphological Catalog of Northern Galactic Planetary Nebulae*, Instituto de Astrofísica de Canarias
- Massey, P., Strobel, K., Barnes, J. V., & Anderson, E. 1988, *ApJ*, 328, 215
- Miranda, L.F., Guerrero, M.A., & Torrelles, J.M. 1999, *AJ*, 117, 1421
- Miranda, L.F., & Solf, J. 1992, *A&A*, 260, 397
- Miranda, L.F., Torrelles, J.M., Guerrero, M.A., Aaquist, O.B., & Eiroa, C. 1998, *MNRAS*, 298, 243
- Miranda, L.F., Vázquez, R., Torrelles, J.M., Eiroa, C., & López, J.A. 1997, *MNRAS*, 288, 777
- Oke, J.B. 1974, *ApJS*, 27, 21
- Peimbert, M. 1990, *Rep. Prog. Phys.*, 53, 1559
- Pereira, C.B., & Miranda, L.F. 2005, *A&A*, 433, 579
- Pereira, C.B., & Miranda, L.F. 2007, *A&A*, 462, 231
- Pereira, C.B., Miranda, L.F., Smith, V.V., & Cunha, K. 2008, *A&A*, 477, 535
- Preite-Martínez, A. 1988, *A&AS*, 76, 317

- Robertson, T.H., & Jordan, T.M. 1989, AJ, 98, 1354
- Sahai, R., Morris, M., Sánchez-Contreras, C., & Claussen, M. 2007, AJ, 134, 2200
- Sahai, R., Trauger, J.T. 1998, AJ, 116, 1357
- Shaver, P.A., McGee, R.X., Newton, L.M., et al. 1983, MNRAS, 204, 53
- Stanghellini, L., Guerrero, M.A., Cunha, K., Manchado, A. Villaver, E. 2006, ApJ, 651, 898
- Vázquez, R., Miranda, L.F., Torrelles, et al. 2002, ApJ, 576, 860

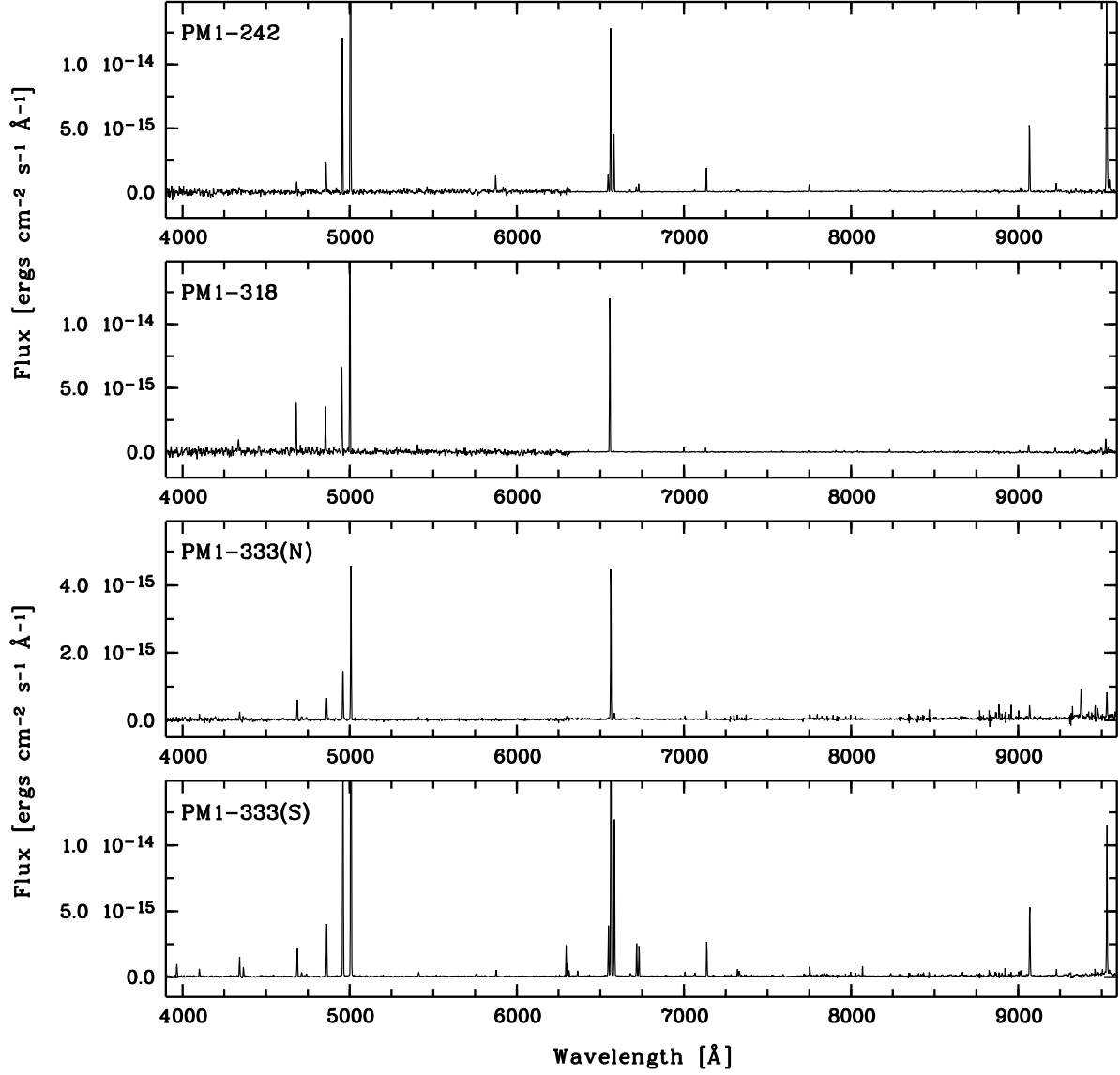


Fig. 1.— Blue and red 2.2m CAHA CAFOS spectra of PM1-242, PM1-318 and PM1-333. In the case of PM1-333, the spectra of two different regions (North and South) within the object are shown (see text).

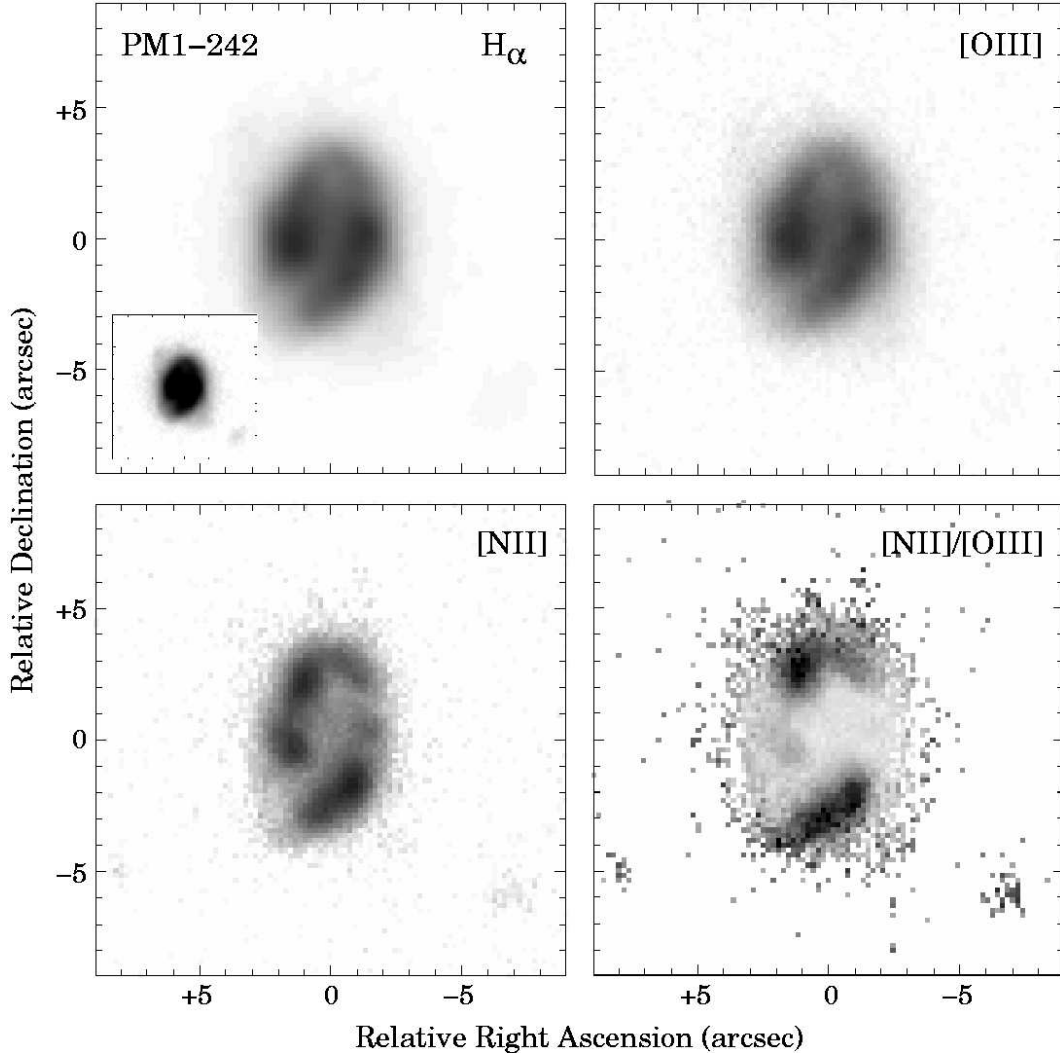


Fig. 2.— Grey-scale representations of the $H\alpha$, [N II] and [O III] images, and [N II]/[O III] image ratio of PM1-242. Grey levels are logarithmic except in the [N II]/[O III] image ratio where they are linear (black represents high values of the ratio). The $H\alpha$ image is shown in the inset with a different grey scale in order to highlight the faint regions of the object. (0,0) corresponds to the geometrical center of the two bright knots oriented east-west in the $H\alpha$ and [O III] images.

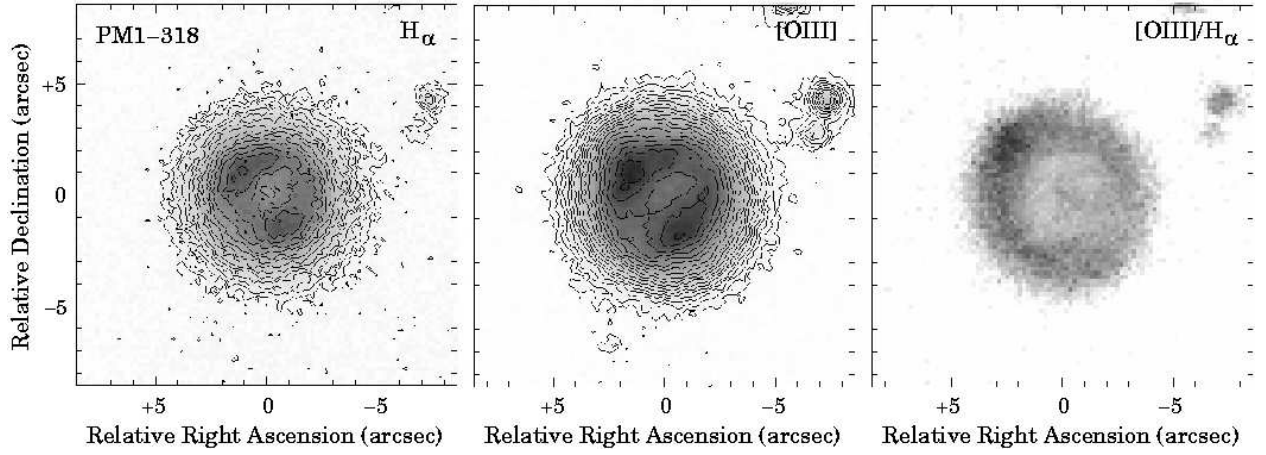


Fig. 3.— Grey-scale and contour representations of the H_{α} and $[O III]$ images, and $[O III]/H_{\alpha}$ image ratio of PM 1-318. The grey levels are linear. Contours are arbitrary and have been chosen to highlight the structure of the nebula. In the $[O III]/H_{\alpha}$ image ratio, black represents high values of the ratio. (0,0) corresponds to the position of the central minimum in the H_{α} image.

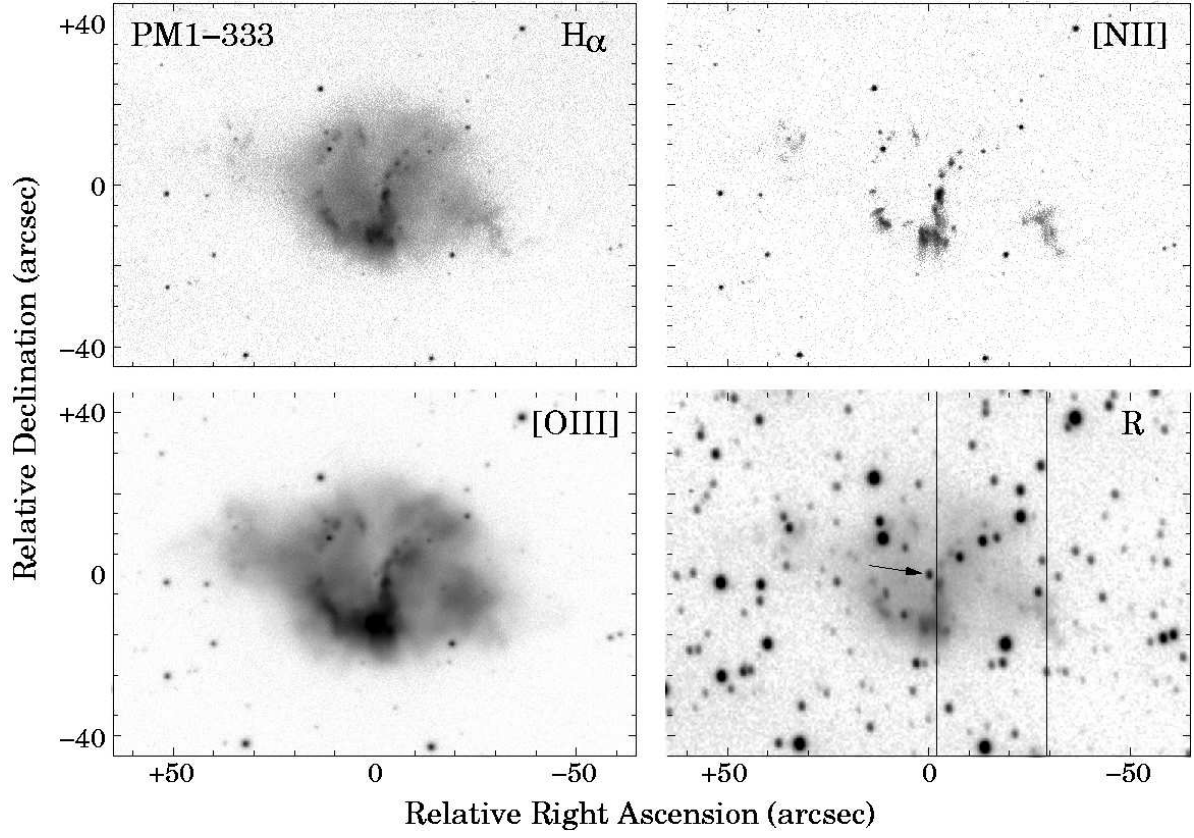


Fig. 4.— Grey-scale representations of the $H\alpha$, [N II], [O III] and R images of PM 1-333. Grey levels are logarithmic. (0,0) corresponds to the position of the candidate central star of the nebula, indicated in the R image by an arrow. The two vertical lines in the R image indicate the two slit positions used for spectroscopy.

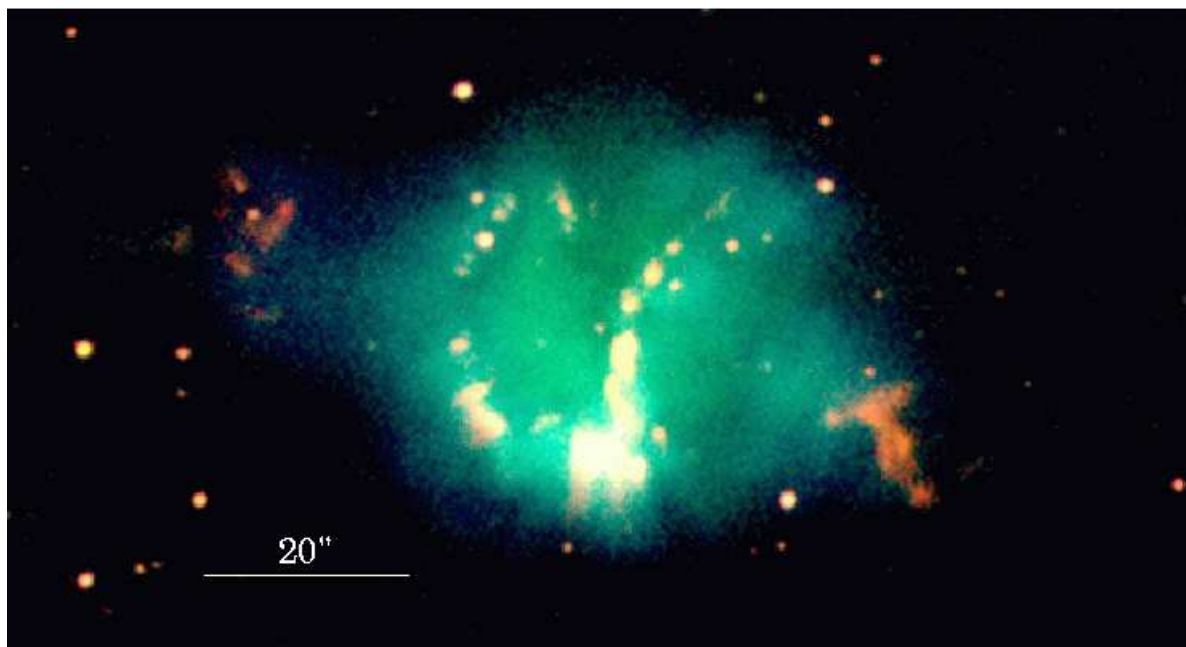


Fig. 5.— Composite colour picture of PM 1-333 constructed with the images shown in Fig. 1. Red corresponds to $[\text{N II}]$, green to $\text{H}\alpha$, and blue to $[\text{O III}]$. North is up, east to the left.

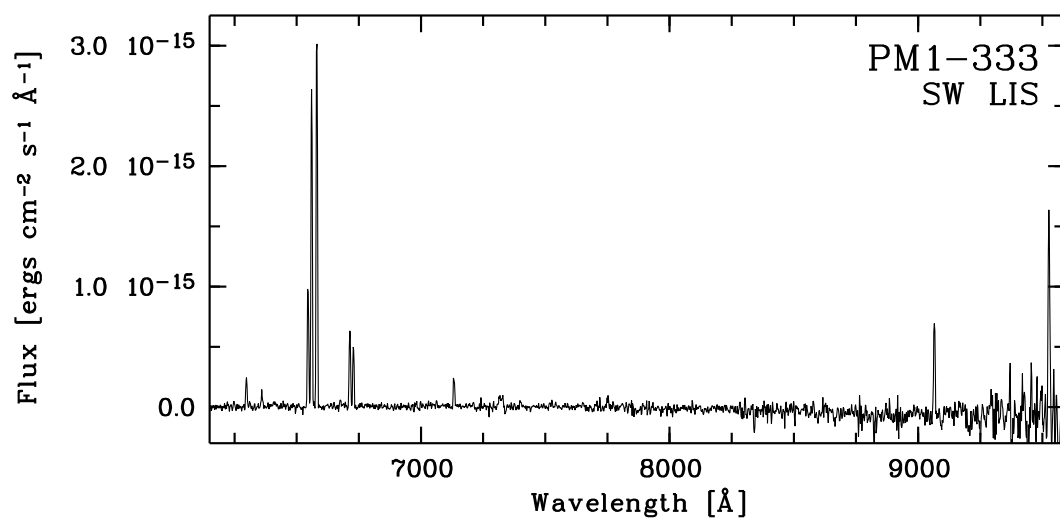


Fig. 6.— Red 2.2m CAHA CAFOS spectrum of the SW low-ionization structure of PM 1-333 (see Fig. 4).

Table 1. Names, coordinates and IRAS colours of PM 1-242, PM 1-318 and PM 1-333

Object	IRAS name	PN G name	α (J2000)	δ (J2000)	[12]–[25]	[25]–[60]
PM 1-242	18320+0005	031.1+03.7	$18^h 34^m 38.7^s$	$+00^\circ 08' 03''$	≥ 1.25	0.71
PM 1-318	20077+3722	074.5+02.3	$20^h 09^m 32.9^s$	$+37^\circ 31' 15''$	≥ 1.22	0.95
PM 1-333	21394+5844	100.4+04.6	$21^h 40^m 59.1^s$	$+58^\circ 58' 37''$	≥ 1.66	0.07

Table 2. Emission line intensities in PM 1-242, PM 1-318 and PM 1-333

Line	f(λ)	PM 1-242	PM 1-318	PM 1-333	PM 1-333	PM 1-333
		I(λ)	I(λ)	(North) I(λ)	(South) I(λ)	(SW-LIS) I(λ)
[O II] λ 3727	0.266	165 \pm 3	...
[Ne III] λ 3869	0.228	86 \pm 20	...	72 \pm 7	123.3 \pm 2.1	...
He I + H8 λ 3889	0.223	17.7 \pm 1.4	...
[Ne III] + He λ 3968	0.203	56.2 \pm 1.4	...
H δ + He II λ 4101	0.172	32 \pm 4	27.0 \pm 1.0	...
H γ λ 4340	0.129	...	41 \pm 5	44.3 \pm 2.3	49.0 \pm 0.9	...
[O III] λ 4363	0.124	23.9 \pm 0.7	...
He II λ 4686	0.042	44 \pm 8	105 \pm 5	92.5 \pm 2.1	60.8 \pm 0.7	...
He I + [Ar IV] λ 4711	0.036	27.0 \pm 1.9	11.2 \pm 0.4	...
[Ar IV] λ 4740	0.029	19.4 \pm 2.1	7.2 \pm 0.4	...
H β λ 4861	0.000	100 \pm 6	100 \pm 6	100.0 \pm 2.0	100.0 \pm 0.8	100.0 \pm 1.2
[O III] λ 4959	-0.023	473 \pm 9	183 \pm 6	227 \pm 3	398.2 \pm 1.4	...
[O III] λ 5007	-0.034	1490 \pm 14	548 \pm 8	642 \pm 4	1189.3 \pm 2.3	...
He II λ 5411	-0.118	...	21 \pm 4	10.7 \pm 1.2	6.6 \pm 0.3	...
[N II] λ 5755	-0.191	4.4 \pm 0.2	...
He I λ 5876	-0.216	36 \pm 3	6.8 \pm 0.2	...
[O I] λ 6300	-0.285	5.4 \pm 0.8	10.8 \pm 0.1	28.9 \pm 1.6
[S III] λ 6312	-0.287	5.8 \pm 0.8	4.6 \pm 0.1	4.2 \pm 0.6
[O I] λ 6363	-0.294	2.6 \pm 0.4	3.7 \pm 0.1	14.6 \pm 1.4
[N II] λ 6548	-0.321	29.8 \pm 0.6	1.3 \pm 0.4	4.4 \pm 0.4	36.8 \pm 0.2	110.6 \pm 1.8
H α λ 6563	-0.323	285.0 \pm 1.4	285.0 \pm 1.6	285.0 \pm 1.4	285.0 \pm 0.5	285.0 \pm 2.3
[N II] λ 6584	-0.326	89.3 \pm 0.8	3.1 \pm 0.3	15.8 \pm 0.5	112.1 \pm 0.3	323.0 \pm 2.3
He I λ 6678	-0.338	4.0 \pm 0.3	3.1 \pm 0.1	5.8 \pm 1.5
[S II] λ 6716	-0.343	8.9 \pm 0.4	22.7 \pm 0.2	68.0 \pm 1.6
[S II] λ 6731	-0.345	12.8 \pm 0.4	20.7 \pm 0.2	49.7 \pm 1.6
[Ar V] λ 7005	-0.376	...	9.3 \pm 0.6
He I λ 7065	-0.383	4.1 \pm 0.3	2.1 \pm 0.1	3.6 \pm 0.9
[Ar III] λ 7135	-0.391	30.9 \pm 0.5	8.7 \pm 0.6	12.7 \pm 0.4	19.7 \pm 0.8	21.7 \pm 1.0
[O II] λ 7319	-0.410	5.2 \pm 0.5	4.1 \pm 0.1	10.7 \pm 1.4
[O II] λ 7330	-0.411	4.3 \pm 0.5	3.4 \pm 0.1	9.2 \pm 1.3
[Cl IV] λ 7529	-0.430	...	1.7 \pm 0.3

Table 2—Continued

Line	f(λ)	PM 1-242	PM 1-318	PM 1-333	PM 1-333	PM 1-333
		I(λ)	I(λ)	(North) I(λ)	(South) I(λ)	(SW-LIS) I(λ)
He II λ 7592	-0.436	...	2.9 \pm 0.6	3.4 \pm 0.4	1.4 \pm 0.1	...
[Ar III] λ 7751	-0.451	10.1 \pm 0.4	3.4 \pm 0.6	8.5 \pm 0.5	5.4 \pm 0.1	6.5 \pm 1.6
[Cl IV] λ 8045	-0.477	2.8 \pm 0.3	2.8 \pm 0.5
He II λ 8236	-0.492	3.0 \pm 0.4	6.2 \pm 0.7
P15 λ 8545	-0.532	0.6 \pm 0.1	...
P14 λ 8598	-0.540	2.1 \pm 0.6	1.0 \pm 0.1	...
P13 λ 8664	-0.550	2.5 \pm 0.6	1.1 \pm 0.1	...
P12 λ 8750	-0.562	3.9 \pm 0.6	0.9 \pm 0.1	...
P11 λ 8862	-0.578	3.8 \pm 0.6	1.3 \pm 0.1	...
P10 λ 9014	-0.599	4.2 \pm 0.7	4.2 \pm 1.2	...	2.0 \pm 0.1	...
[S III] λ 9069	-0.606	71.6 \pm 1.0	15.6 \pm 1.1	16.5 \pm 0.5	28.4 \pm 0.2	44.0 \pm 2.1
P9 λ 9228	-0.612	10.0 \pm 0.7	11.4 \pm 1.8	...	2.2 \pm 0.1	...
[S III] λ 9532	-0.620	267.0 \pm 2.4	28 \pm 3	28.8 \pm 1.1	51 \pm 5	100 \pm 7
P8 λ 9546	-0.620	14.6 \pm 1.2	2.2 \pm 0.1	...
c(H β)		0.90	0.13	0.97	1.19	1.19 ^a
log F _{Hβ} (erg cm ⁻² s ⁻¹)		-13.93	-13.75	-14.43	-13.69	-14.59

^aAssumed to be identical to the value in PM 1-333 South (see text)

Table 3. Ionic abundances relative to H^+ in PM 1-242 and PM 1-333 South

Ion ^a	PM 1-242	PM 1-333 South
He^+	0.24 ± 0.02	0.06 ± 0.01
He^{+2}	0.05 ± 0.01	0.07 ± 0.01
O^0	$1.11 \pm 0.37 \times 10^{-5}$	$5.18 \pm 0.23 \times 10^{-6}$
O^+	$7.62 \pm 4.73 \times 10^{-5}$	$1.47 \pm 0.14 \times 10^{-5}$
O^{+2}	$4.71 \pm 1.27 \times 10^{-4}$	$1.20 \pm 0.04 \times 10^{-4}$
N^+	$1.67 \pm 0.35 \times 10^{-5}$	$8.11 \pm 0.26 \times 10^{-6}$
Ne^{+2}	$8.61 \pm 3.50 \times 10^{-5}$	$3.27 \pm 0.16 \times 10^{-5}$
S^+	$6.66 \pm 1.89 \times 10^{-7}$	$4.44 \pm 0.17 \times 10^{-7}$
S^{+2}	$1.27 \pm 0.20 \times 10^{-5}$	$1.97 \pm 0.11 \times 10^{-6}$
Ar^{+2}	$2.92 \pm 0.53 \times 10^{-6}$	$7.92 \pm 0.52 \times 10^{-7}$
Ar^{+3}	...	$5.73 \pm 0.36 \times 10^{-7}$
Cl^{+3}	$1.94 \pm 0.40 \times 10^{-7}$...

^aFor ions with more than one transition, a flux-weighted average was obtained

Table 4. Elemental abundances in PM 1-242, PM 1-333 South and other objects

Element ratio	PM 1-242 ^a	PM 1-333 (S) ^a	Type I PNe ^b	Type II PNe ^c	H II regions ^d	Sun ^e
He/H	0.29	0.13	0.13	0.11	0.10	0.09
O/H ($\times 10^4$)	6.21	2.25	4.47	5.13	5.01	4.57
N/H ($\times 10^4$)	1.36	1.24	5.25	1.58	3.71	6.02
S/H ($\times 10^5$)	4.66	1.05	0.81	0.60	1.15	1.38
Ar/H ($\times 10^6$)	5.46	1.36	2.63	2.54	2.63	1.51
Ne/H ($\times 10^4$)	1.13	0.61	1.23	1.17	0.79	0.69
N/O	0.22	0.55	1.17	0.31	0.07	0.13

^aSee §3.1 and §3.3.2 for a discussion on the errors

^bAverage for Type I PNe (Kingsburgh & Barlow 1994)

^cAverage for Type II PNe (Henry et al. 2004)

^dAverage for H II regions (Shaver et al. 1983)

^eThe Sun (Grevesse et al. 2007)